nature energy

Article

https://doi.org/10.1038/s41560-025-01811-y

# Monolithic gyroidal solid oxide cells by additive manufacturing

Received: 18 January 2025

Accepted: 4 June 2025

Published online: 18 July 2025

Check for updates

Zhipeng Zhou[1] ✉, Aakil R. Lalwani[2], Xiufu Sun[1], Zhihao Pan[2], Pouya Shahriary[1], Yun Xie[1], Yijing Shang[1], Javier L. Navas[2], Alberto Basso[2], Naiqi Shang[2], Marina Artemeva[2], Peyman Khajavi[1], Ming Chen[1], Victor B. Tinti[1], David B. Pedersen[2], Venkata K. Nadimpalli[2] ✉ & Vincenzo Esposito[1] ✉

Solid oxide cells (SOCs) efficiently interconvert chemicals and electricity. However, they are primarily confined to 2D design and fabrication technologies. Planar SOC stacks require complex multi-material components, leading to reduced compactness and high specific weight. Here we escape the 2D paradigm and adopt a true 3D design based on triply periodic minimal surface structures, enabling superior performance on gravimetric and volumetric bases. Leveraging the resolution and accuracy of additive manufacturing, we demonstrate a monolithic, gyroidal SOC that eliminates the need for metallic interconnects and sealing components. The monolith achieves optimal spatial utilization, exceptional mass-specific indexes, a straightforward manufacturing procedure and high electrochemical and thermomechanical stability. The specific power and volumetric power density surpass 1 W $g^{-1}$ and 3 W $cm^{-3}$ in fuel cell mode, and the mass-index and volume-index hydrogen production rates are about $7 \times 10^{-4}$ $Nm^3$ $h^{-1}$ $g^{-1}$ and $2 \times 10^{-3}$ $Nm^3$ $h^{-1}$ $cm^{-3}$ in electrolysis mode, nearly an order of magnitude enhancement compared to planar stacks.

Solid oxide cells (SOCs) offer a highly efficient platform for electrochemical energy conversion, operating at high temperatures (above 600 °C) to transform chemical energy into electricity and vice versa reversibly[1,2]. In fuel cell mode (SOFC), it achieves electrical efficiencies of up to 65% and total system efficiencies exceeding 90% in combined heat and power[2,3]. In electrolysis mode (SOEC), it converts electricity into fuel gases (*X*), oxygen and heat, enabling Power-to-*X* applications[1]. These attributes make SOCs attractive for stationary power generation[4,5] and emerging applications in aeronautics and space exploration[6–8].

Despite their advantages, conventional SOC stack designs impose significant limitations on mobility and system integration. Metallic interconnects and sealing components account for over 75% of stack weight[7], restricting power density and increasing structural complexity. The effective specific area (ESA) of planar and tubular SOC stacks is typically below 50 $mm^2$ $g^{-1}$ and 0.12 $mm^2$ $mm^{-3}$, translating to specific power and volumetric power densities below 0.2 W $g^{-1}$ and 1 W $cm^{-3}$ (refs. 9–17). While offering improved mechanical stability, tubular stacks suffer from even lower space utilization[16] unless specialized designs, such as spiral configurations[18], are adopted. Meanwhile, metallic components in SOC stacks are prone to oxidation and degradation under high-temperature operation, limiting long-term stability. Despite decades of development, SOCs remain largely confined to planar or tubular configurations[19], with incremental improvements constrained by conventional manufacturing techniques.

Additive manufacturing (AM) presents a pathway to overcome these limitations by enabling complex geometries and novel architectures[20]. High-resolution ceramic AM methods, including stereolithography[21] and digital light processing (DLP)[22], facilitate the precise structuring of ceramic slurries, which are then sintered

[1]Department of Energy Conversion and Storage, Technical University of Denmark, Kongens Lyngby, Denmark. [2]Department of Civil and Mechanical Engineering, Technical University of Denmark, Kongens Lyngby, Denmark. ✉e-mail: zhipeng.zhou@polyu.edu.hk; vkna@dtu.dk; vies@dtu.dk

https://doi.org/10.1038/s41560-025-01811-y

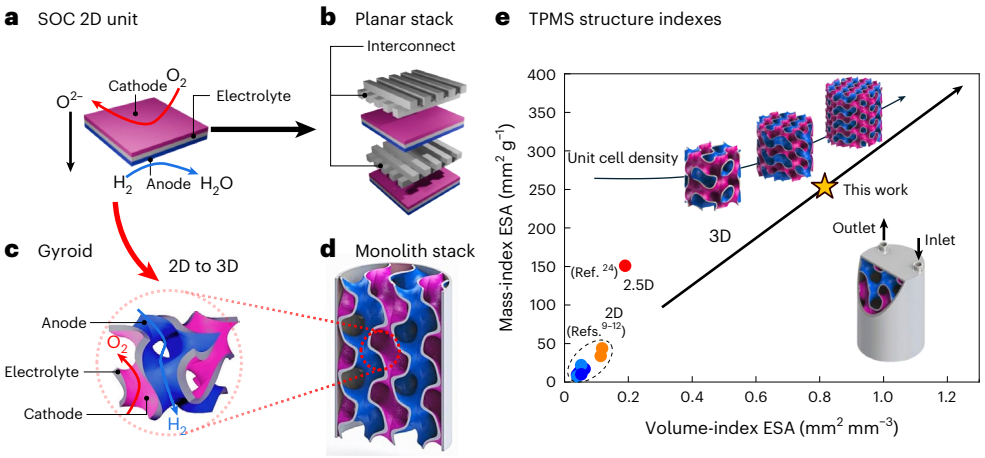


**Fig. 1 | Planar vs 3D SOC. a**,**b**, Typical planar (2D) SOC and stack design (taking the SOFC mode as an example), including single cells (**a**) and interconnects in the stack (**b**). **c**,**d**, 3D monolithic SOC design, including the gyroidal structural unit (**c**) and the monolithic stack (**d**) obtained through periodic multiplication, is enclosed in a shell separating the fuel and oxidant sides. **e**, Structural advantages of 3D SOCs compared with conventional planar SOC stacks[9–12] and the 2.5D design[24]. ESA is the effective specific area. The mass of all functional layers of 3D SOCs has been factored into the calculation. Please refer to Supplementary Note 2 for calculating the effective area of the 3D SOC.The data enclosed by the dashed outline pertains to 2D SOC stacks.

into dense, functional components. AM-enabled SOC designs have demonstrated promising advancements[23–25]. For instance, stereolithography-fabricated corrugated electrolytes increase the effective surface area by 60% within the same footprint[25], thereby straightforwardly achieving the monolithic SOC concept[26] proposed in the 1990s. However, this design remains constrained by conventional 2D stacking paradigms, with limitations in reducing stack weight and enhancing compactness due to the required use of metallic interconnects. Another design integrates multiple tubular shapes into a single one-piece stack using the stereolithography process[24]. As a result, the metallic interconnects can be avoided, thereby reducing weight (calculated as ≈150 $mm^2\ g^{-1}$). This solution highlights the ability of AM technology to produce stacks, advancing the concept of SOC from 2D to 2.5D. Nevertheless, the tubular structure has a low space utilization; thus, its contribution to enhancing compactness is limited ($\approx 0.19\ mm^2\ mm^{-3}$). Furthermore, neither the corrugated[25] nor the tubular[24] designs fall under the electrolyte-supported category. The electrolytes are 270-µm-thick to ensure sufficient mechanical strength, which limits the electrochemical performance of the SOC due to the considerable ohmic resistance caused by the thick electrolyte.

Here we present a fully 3D monolithic SOC architecture that eliminates metallic interconnects and sealing components. This true 3D design optimizes spatial utilization and electrochemical and thermomechanical stability while simplifying manufacturing. As a result, the system surpasses 1 W $g^{-1}$ and 3 W $cm^{-3}$ in fuel cell mode, and it achieves hydrogen production rates of approximately $7 \times 10^{-4}$ $Nm^3\ h^{-1}\ g^{-1}$ and $2 \times 10^{-3}$ $Nm^3\ h^{-1}\ cm^3$ in electrolysis mode—nearly an order of magnitude improvement over conventional SOC stacks. These findings establish a unique paradigm for SOC technology, opening avenues for more compact, lightweight and scalable energy systems.

## Monolithic gyroidal SOC design

The monolithic gyroidal SOC concept is represented in Fig. 1. The schematics also compare the planar configuration with the proposed triple periodic minimal surface (TPMS) design. The latter is based on the complex geometry of gyroidal symmetry, that is, one of the TPMS symmetries[27]. TPMSs are mathematical functions that define orientable, self-intersection-free 3D surfaces. These surfaces divide space into two disjoint sub-volumes, called labyrinths, and have two independent channels separated by a curved thin wall. The gyroidal surface is a homogeneous balance surface with zero mean curvature[28], defined by the equation:

$$\sin(x)\cos(y) + \sin(y)\cos(z) + \sin(z)\cos(x) = 0 \quad (1)$$

Benefiting from the substantially higher space utilization of the TPMS structure compared with the conventional planar structure, the TPMS structure has been conceptualized and reported to be utilized in lithium-ion batteries for a significant boost in their energy density[29,30]. In addition, relying on the high mass and heat transfer efficiency of the TPMS structure, it has been conceived as the structure for the next-generation heat exchanger[31]. These characteristics are in perfect alignment with the working concept of SOCs. Due to its high space utilization and adjustable volumetric density, the monolithic gyroidal SOC is distinguished from 2D and 2.5D designs. In the 3D SOC, the TPMS isolated channels inherently satisfy the gas supply requirements. The monolithic concept is achieved by replicating the gyroid units and adding a sealed shell frame called the outer shell to maintain gas-tight conditions. Further details on the monolith design and fabrication can be found in Supplementary Fig. 1.

The electrolyte and sealing shell form the self-supporting framework of the 3D SOC. The monolith is fabricated in 8 mol% yttria-stabilized zirconia (8YSZ) using an open-source DLP-based AM system[22]. To meet the functional requirements of SOC, the fuel electrode and oxygen electrode are coated on the respective surfaces of the gyroidal electrolyte (Fig. 1c). The 3D gyroidal structure enhances the monolith's compactness, achieving a fourfold increase in volume-index ESA and a sixfold increase in mass-index ESA compared to conventional SOC stacks (Fig. 1e). In the gyroidal SOC design, space utilization or compactness, is highly tunable. Compactness can be improved by increasing the density of the gyroid units (units per $cm^3$). Examples are shown in Supplementary Note 1 and Supplementary Fig. 2. The gyroid unit density for this study is set to 16 units per $cm^3$.

The high resolution (pixel size is 7.54 µm) and stability of the DLP-based AM system is demonstrated through the structural characterization of the samples. Figure 2a shows the 3D-printed 8YSZ electrolytes after heat treatments. The sample within the red dashed box (Fig. 2a) does not have top and bottom sealing covers to show the internal structure and measure the actual thickness of the electrolyte (Fig. 2c). We reduced the 8YSZ electrolyte thickness to below 150 µm, approximately half the thickness of other 3D-printed electrolytes[24,32] and less than 75% of the thickness found in electrolyte-supported designs[33]. Optical microscopy (OM), X-ray micro-computed tomography (µCT) and scanning electron microscopy (SEM) are used to identify any manufacturing defects (Fig. 2b–f).

https://doi.org/10.1038/s41560-025-01811-y

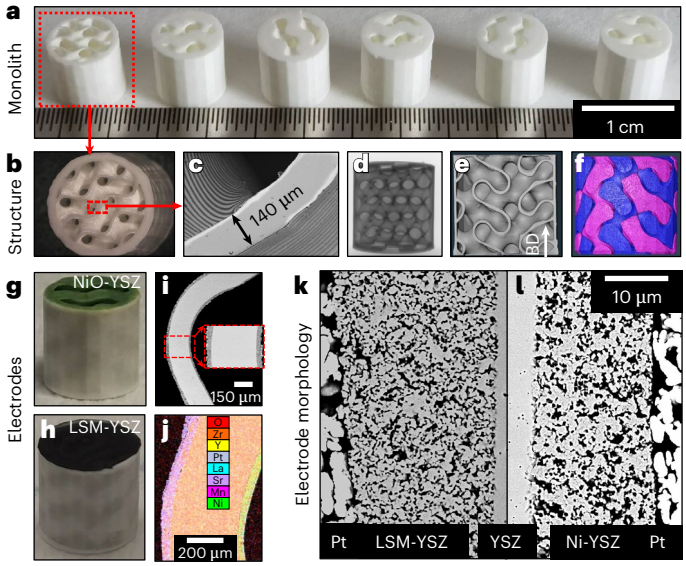


**Fig. 2 | Structural characterization of the 3D SOC. a**, Sintered 8YSZ SOC electrolytes with a shell. **b**, Optical microscope image of the gyroid structure. **c**, SEM image of the gyroid's thin-wall structure. **d**, A typical X-ray projection of the monolith. **e**, Cross section along the building direction (BD) of the µCT-reconstructed 3D structure. **f**, Porosity distribution of the µCT-reconstructed 3D structure, with interconnected pores represented in the same colour. **g**,**h**, Morphology of the monolith after co-sintering with the coated NiO-YSZ fuel electrode (**g**) and filling with LSM-YSZ slurry (**h**). **i**,**j**, Cross section perpendicular to the BD showing SEM morphology (**i**) and EDS mapping (**j**) of a typical tested sample, featuring a coated fuel electrode (Ni-YSZ), oxygen electrode (LSM-YSZ) and current collector (Pt). **k**,**l**, Microstructure of the LSM-YSZ (**k**) and Ni-YSZ electrodes (**l**). Note that the SEM of **c** presents the actual thickness of the electrolyte. The actual thickness of the electrolyte can only be observed when the cross section intersects the electrolyte perpendicularly.

Under optical microscopy, the samples exhibit an intricate and fine structure, with the printed design aligning precisely with the intended shape. No surface manufacturing defects are observed. The SEM-measured thickness of the sintered gyroid electrolyte is approximately 140 µm, closely matching the calculated value of 148 µm based on previously measured shrinkage along the *X* or *Y* direction (about about 27%). The hollow structure within the sintered sample is visible under X-ray projection (Fig. 2d). Three-dimensional reconstruction reveals the internal gas channels, with no signs of penetrating defects such as cracks and delamination being detected (Fig. 2e,f). The samples exhibited high relative density (about 99% of the nominal density), comparable to commercial 8YSZ ceramic plates (Supplementary Fig. 3a). Meanwhile, the ionic conductivity of the samples is also comparable to that of commercial 8YSZ electrolytes (Supplementary Fig. 3d).

The fuel electrode made of NiO-YSZ and the oxygen electrode composed of LSM-YSZ are coated using a wet chemical technique (Supplementary Fig. 4a). Figure 2g shows a sample coated only with the NiO-YSZ electrode. The outer surface of the sample displays a distinct contrast between the NiO-YSZ-coated channels and the empty channels, confirming that the gyroid electrolyte successfully separates the two channels. Figure 2h shows an example where one of the channels was filled with LSM-YSZ slurry, demonstrating the structural integrity of the sintered 8YSZ frame (no leakage). The electrodes fully cover the electrolyte's surface and form a strong bond with the intricately textured electrolyte after co-sintering. Layers of Pt are coated on the electrode surfaces and as current collectors, with the Pt distribution shown in the EDS map. Yet the bonding between each functional layer remains intact after electrochemical testing, indicating the monolith's excellent thermo–chemo–mechanical performance and stability. Figure 2i shows the detailed SEM morphology sliced along the horizontal section, revealing good bonding between the functional layers. It should be noted that during the electrode coating process (Supplementary Fig. 4a), the thickness of the electrodes is influenced by the gas flow rate and the pressure. The local shape of the electrolyte affects the airflow, consequently leading to uneven electrode thickness. The findings of the µCT analysis regarding the macroscopic distribution of the electrodes are shown in Supplementary Fig. 4b–d.

## Electrochemical performance

Electrochemical tests are carried out in both SOFC and SOEC modes on different samples for reproducibility (Fig. 3). Nearly identical electrochemical impedance spectroscopy (EIS) characteristics indicate the good process stability and consistency of the 3D SOC manufacturing method (Fig. 3c,e). The samples are mounted on a planar zirconia platform and loaded under a weight with gold sheets to ensure sealing (Fig. 3a and Supplementary Fig. 5). The 3D SOCs achieved the desired area power density of over 450 mW $cm^{-2}$ at 900 °C in the SOFC mode (Supplementary Fig. 6a) and a current density of over 650 mA $cm^2$ at 900 °C in the SOEC mode.

The typical Nyquist plots from EIS measurements for SOFC and SOEC are shown in Fig. 3c,e. The well-defined semi-arcs indicate a high-quality bonding interface between the electrodes and the electrolyte. This result further confirms the successful integration of the distinct functional layers within the monolith, anchored by the gyroid surfaces. These results validate the effectiveness of our design, 3D printing system and wet chemical coating method for SOC fabrication.

The specific power of the 3D SOFC exceeds the threshold required for aerospace applications, reaching over 1 W $g^{-1}$ (ref. 7). Compared to conventional planar SOFC stacks (Fig. 3g and Supplementary Fig. 6b), the specific power and volume power density have been significantly improved by factors 7 and 9, respectively, as shown in Fig. 3g. Additionally, when compared to conventional planar SOEC stacks[34,35], the $H_2$ production rate of the 3D SOEC per gram (mass-index) and cubic centimetre (volume-index) increases by nearly an order of magnitude (Supplementary Table 1). These characteristics are crucial for demanding applications such as space exploration, including NASA's Mars project[8]. Current plans involve deploying planar SOEC stacks with a total weight of 6,400 kg and volume of 6,600 l to produce oxygen for human activities on Mars[8], presenting significant challenges and costs for launch and transportation. Scaling up 3D SOC stacks by integrating independent monoliths could achieve equivalent performance with devices in the 800 kg and 700 l range.

The gas tightness of the 3D SOC is reflected in its stability, as indicated by continuous monitoring of the open-circuit voltage (Supplementary Fig. 6c). The measured open-circuit voltage is 1.06 V at 800 °C with room-temperature humidified $H_2$ supplied to the fuel electrode and $O_2$ supplied to the oxygen electrode. This value is approximately 50 mV lower than the theoretical voltage calculated using the Nernst equation, with the slight difference probably due to imperfect sealing of the external gas connections during testing. The test house adapted for the monolith requires additional sealing in the fuel compartment, originally designed for planar samples and not customized for the 3D geometry (Supplementary Fig. 5). The columnar shape of the 3D SOC, with its high height-to-width ratio, can exert uneven pressure on the seal ring, resulting in inadequate sealing.

The monoliths also operate in SOFC and SOEC modes under galvanostatic conditions for hundreds of hours (Fig. 4). The current value is set based on the typical operating voltage of 0.7 V for SOFC and 1.3 V for SOEC. The 3D SOCs demonstrated exceptional, reliable and steady operation, with degradation rates comparable to SOCs made from the same materials under similar testing conditions[32,36]. The area-specific resistance of the 3D SOFC increased by approximately 11%, and that of the 3D SOEC increased by around 8% (Supplementary Fig. 7a,b). This effect could be ascribed to microstructural changes in the electrodes[37–39]. However, no coarsening or migration of nickel

https://doi.org/10.1038/s41560-025-01811-y

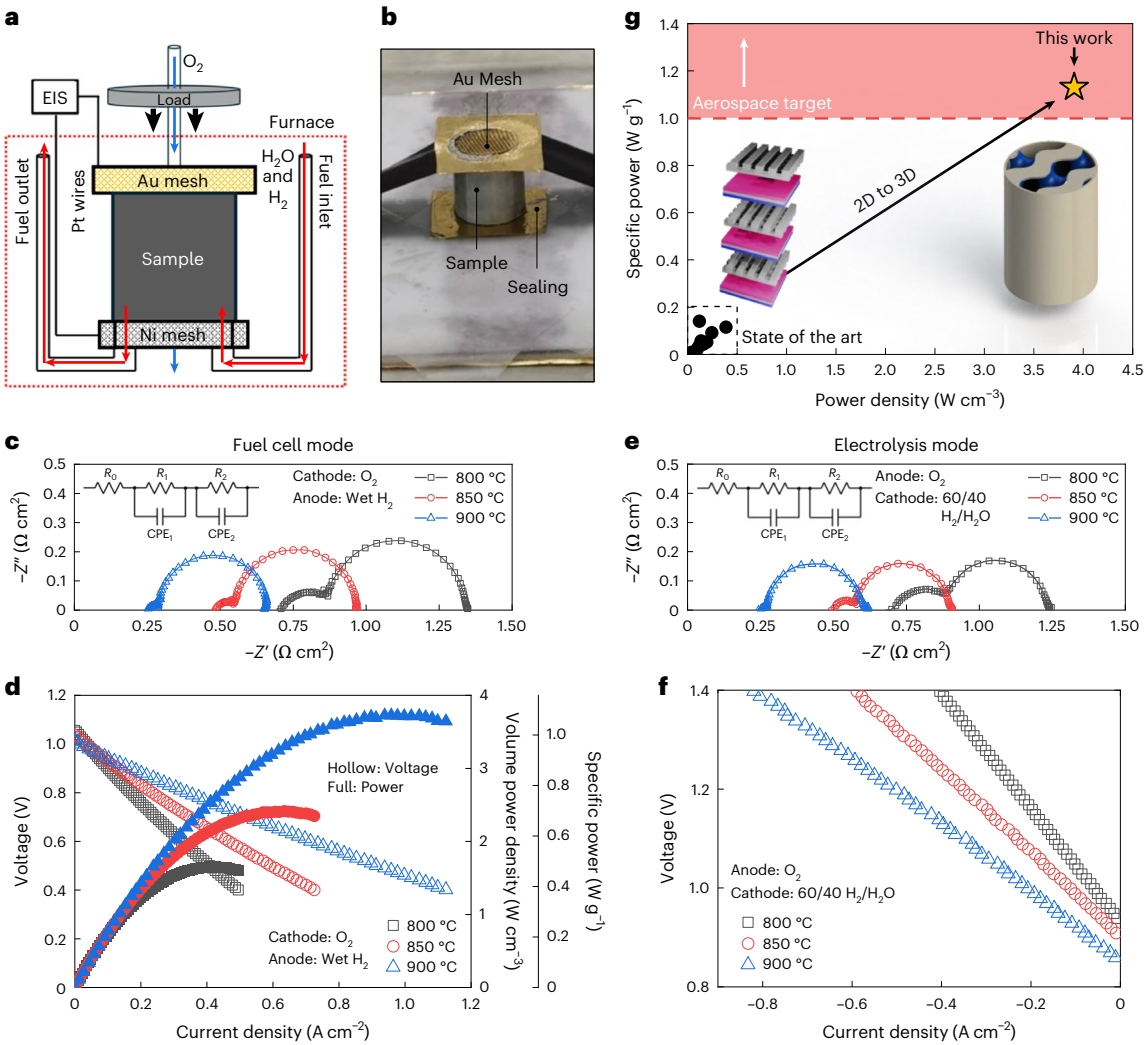


**Fig. 3 | 3D SOC electrochemical performance. a**, Diagram of the experimental set-up for electrochemical testing. **b**, The photo corresponds to **a**, illustrating the placement of the sample. **c**, Nyquist plots of the SOFC. **d**, *I*–*V*–*P* (current–voltage–power) curves of the SOFC. **e**, Nyquist plots of the SOEC. **f**, *I*–*V* curves of the SOEC. **g**, Comparison with the conventional SOFC stacks[9–12,14]. Nyquist plots were measured at open-circuit voltage for the SOFC and at a current of 0.8 A for the SOEC. At 0.8 A, the corresponding voltages are 1.3 V at 800 °C, 1.17 V at 850 °C and 1.07 V at 900 °C. Wet hydrogen at a rate of 4.7 l $h^{-1}$ was supplied to the fuel electrode (anode) of the SOFC. A mixture of 60% hydrogen and 40% steam, also at 4.7 l $h^{-1}$, was supplied to the fuel electrode (cathode) of the SOEC. The oxygen electrodes of both the SOFC and SOEC were exposed to oxygen at a gas supply rate of 30 l $h^{-1}$. Supplementary Fig. 6b provides details in the dashed frame of **g**.

particles was detected (Supplementary Fig. 7c–f). Significant microstructural changes typically require a longer operating time (over 1,000 h) and can be quantified using three-dimensional reconstruction methods[40].

In addition to its high stability under steady-state operation, the monolith also demonstrates exceptional dynamic stability, reflecting its ability to adapt to shifts in operating conditions. A SOC with robust dynamic stability can handle more complex operational environments and increased usage demands. This is particularly important in harsh environments where unstable operating conditions are common. Figure 4c shows the monolith operating in reversible mode. The system transitions between antidromic modes from SOFC to SOEC every 10 h. After five cycles, it maintains stable SOEC operation under galvanostatic control without any instances of failure. No delamination between the functional layers was observed, as shown in Supplementary Fig. 8. Figure 4d illustrates the 3D SOEC system operating under galvanostatic control with temperature fluctuations. The temperature varied by 100 °C (from 800 to 900 °C), with the maximum rate of temperature change of 5 °C $min^{-1}$. After six heating and cooling cycles, the 3D SOEC continued steady, showing thermo–electro–chemo–mechanical stability.

## Mechanical stability

Electrolyte-supported planar SOCs of conventional designs typically require a thick 8YSZ electrolyte ( ≥ 200 µm) to ensure mechanical strength for stable operation[24,25,32,33]. Although thick electrolytes increase mechanical robustness, they limit the electrochemical performance of SOCs, increasing the ohmic losses. Planar SOC stacks generally suffer mechanical stress primarily from thermal expansion mismatch between ceramic layers and metallic components[41].

In our tests, the gyroidal SOCs, featuring approximately 148-µm-thick electrolyte, demonstrate high mechanical robustness, maintaining stability during steady-state and dynamic conditions. The fully ceramic monolithic design does not suffer from the thermal expansion mismatch between ceramic layers and metallic components. Moreover, the mechanical robustness can be further improved by tuning the thickness of the outer shell enclosing the gyroidal cell. Figure 5 illustrates the experimental and simulated mechanical features of the monolith. Figure 5a shows that the gyroidal elements of 148 µm with no outer shell have high mechanical resistance to compression comparable with the enclosed 220-µm-thick outer shell. These values meet the mechanical requirements when an 8-kg load is applied to the

https://doi.org/10.1038/s41560-025-01811-y

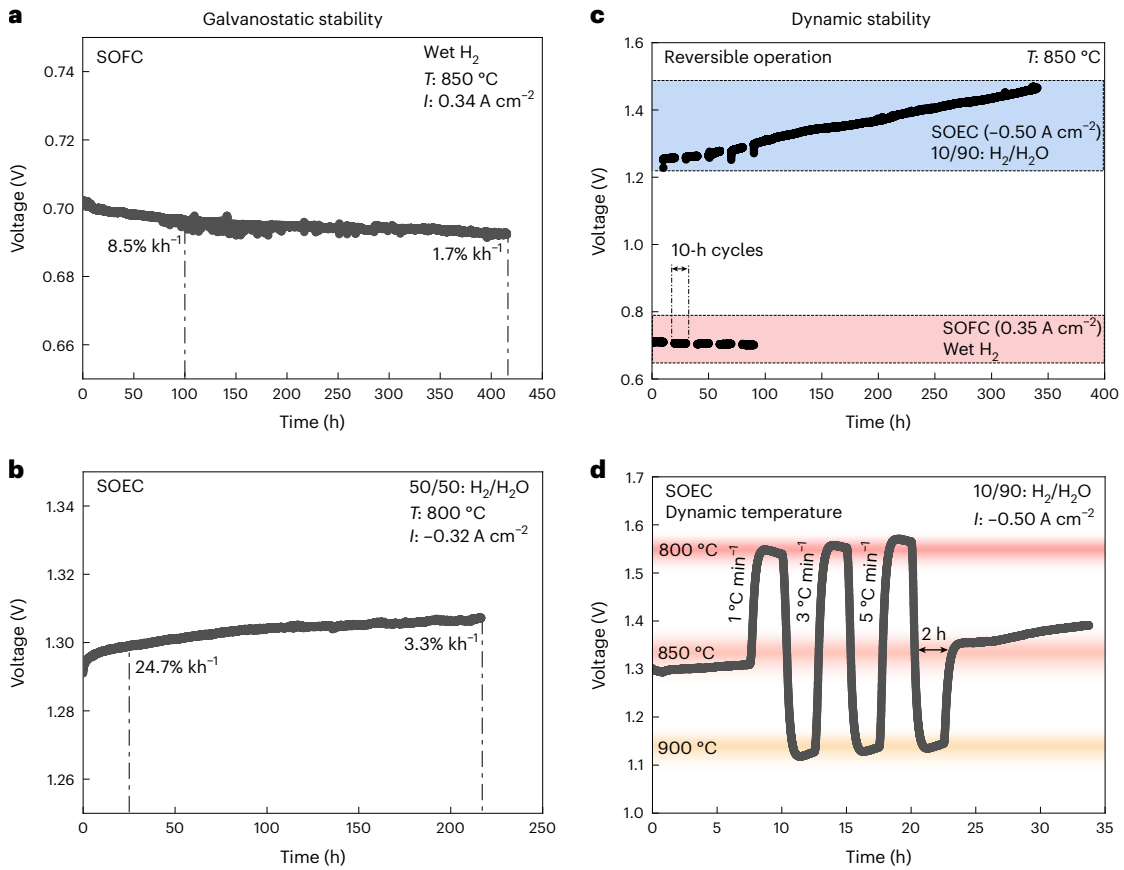


**Fig. 4 | Stability tests. a**, Galvanostatic mode SOFC test, showing the degradation rates of 8.5% kh$^{-1}$ (conditioning phase: <100 h) and 1.7% kh$^{-1}$ (stable phase: >100 h), under the following test conditions: constant discharge current = 0.86 A (≈ 0.34 A cm$^{-2}$); wet hydrogen flow rate = 4.7 l h$^{-1}$; temperature = 850 °C. **b**, Galvanostatic mode SOEC test, showing the degradation rates of 24.7% kh$^{-1}$ (< 25 h) and 3.3% kh$^{-1}$ (> 25 h): constant charge current = 0.80 A (≈ 0.32 A cm$^{-2}$); a mixture of 50% hydrogen and 50% steam flow rate = 3.8 l h$^{-1}$; temperature = 800 °C. **c**, Reversible cycling operations, galvanostatic mode SOFC test: constant discharge current density = 0.35 A cm$^{-2}$; wet hydrogen flow rate = 4.7 l h$^{-1}$; galvanostatic mode SOEC test: constant charge current density = 0.5 A cm$^{-2}$; a mixture of 10% hydrogen and 90% steam flow rate = 2.1 l h$^{-1}$; temperature = 850 °C. Coloured shading refers to the SOEC mode (blue) and the SOFC mode (red). **d**, SOEC operation is conducted with galvanostatic control under varying temperature conditions: constant charge current density = 0.5 A cm$^{-2}$; a mixture of 10% hydrogen and 90% steam flow rate = 2.1 l h$^{-1}$. The oxygen electrodes of SOFCs and SOECs were exposed to oxygen at a gas supply rate of 30 l h$^{-1}$. Coloured shading refers to different operational temperatures.

3D SOCs for sealing during testing. Mechanical performance increases substantially when the support thickness increases, as a 440-µm outer shell achieves about five times the critical stress values.

We use finite element simulations to estimate the impact of reducing the thickness of the electrolyte and increasing that of the support to estimate how the thickness of the electrolyte and the shell affect the overall mechanical resistance and provide insights into the mechanical stress within the gyroid structure. Figure 5b shows that stress concentration on the electrolyte increases as the electrolyte thickness decreases but decreases as the support thickness increases. Moreover, the regions of maximum stress change position within the structures (red areas; Fig. 5b insets). Notably, such a feature indicates no specific critical regions for stress concentration, thus opening multiple design optimization solutions on the entire geometry for mechanical reinforcement. Moreover, compared to conventional SOCs or 3D-printed corrugated SOCs[22], the gyroidal structure mathematically features a zero mean curvature at every point, thus inherently ensuring uniform stress distribution in the large 3D space rather than on a constrained 2D or 2.5D surface[28]. Another important advantage arises from the flexibility in adjusting the outer shell design, which is not electrochemically active, and how the thickness of the shell relieves the potential critical stress gathering in connection with the transition from the gyroidal electrolyte to the outer shell support.

In Fig. 5c, we estimate the effect of outer shell and gyroid thickness and how this changes the stress distribution along the structure. The simulation shows that thicker shells induce a uniform stress distribution on the gyroid electrolyte, both in terms of tensile (Fig. 5d) and shear stress (Fig. 5e). Notably, the latter is typically considered the most critical as it leads to electrode–electrolyte delamination in the planar design. Therefore, the electrolyte and the outer shell can be designed to relieve stress within the gyroid structure, further reducing electrolyte thickness below 100 µm. Such a reduction can substantially enhance electrochemical performance by reducing the ohmic loss and enabling lower operative temperatures. The mechanical properties of SOCs can thus be finely tuned by matching the thickness of the electrolyte and their connection with the outer shell to lead to an optimized design with superior electrochemical and mechanical properties.

## Conclusions

We demonstrate that the 3D gyroidal monolith with TPMS structure offers a wider perspective on SOC design criteria with improved thermo–electro–chemo–mechanical properties. Primarily, the design results in reduced weight and improved space utilization. The high spatial utilization of the gyroid electrolyte is integrated into a sealed outer shell framework, eliminating metallic interconnects. The monolith shows an improvement of nearly an order of magnitude in electrochemical

https://doi.org/10.1038/s41560-025-01811-y

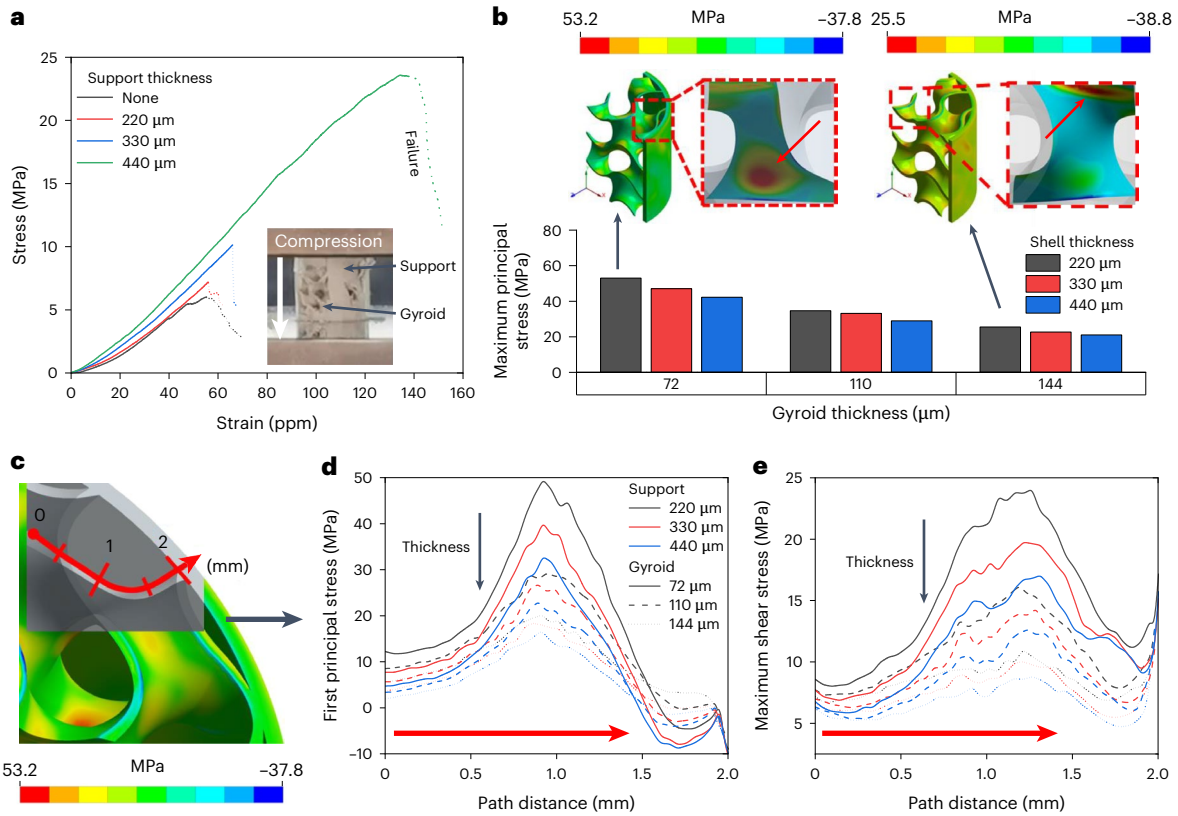


**Fig. 5 | Mechanical properties. a**, Stress–strain ($\sigma_c$–ε) curve during compression. **b**, Maximum value of the first principal stress in the gyroid structure with various electrolyte and support thicknesses. The insets show the geometrical distribution of stress for two examples: a shell support thickness of 220 µm and an electrolyte gyroidal thickness of 72 µm (left) and a shell support thickness of 220 µm and an electrolyte gyroidal thickness of 144 µm (right). **c**–**e**, The indication (**c**) for the reading of the distribution of first principal stress (**d**) and maximum shear stress (**e**) along the gyroid-support contact region under a 10 kg load (sealing load).

performance regarding the weight and volume indices compared to planar SOC stacks. The absence of metallic interconnects also leads to a uniform coefficient of thermal expansion, contributing to excellent mechanical stability during thermal cycling and the reversibility between Power to *X* and *X* to Power. The degradation issues associated with metallic interconnects in conventional SOC stacks have also been removed.

The 3D SOC manufacturing process is simplified compared to conventional stack technology, requiring only three main steps, that is, additive manufacturing, electrode coating and sintering/co-sintering. This approach reduces the complexity of integration and packaging, making the design more suitable for customized energy conversion devices and on-site manufacturing.

Furthermore, the scaling up of the 3D SOC can attain an extraordinarily high degree of design freedom. The representative designs are depicted in Supplementary Fig. 9. The current collection and gas supply challenges arising from channel growth can be circumvented by integrating 3D SOC units (Supplementary Fig. 9b) rather than directly increasing the unit's dimensions (Supplementary Fig. 9a). A more compact design can be attained by modifying the shape of the unit. An illustrative example is presented in Supplementary Fig. 9c. All scaling-up strategies avoid using metallic interconnects.

Finally, our analysis also shows that the design has great potential for further optimization. Notably, the electrolyte thickness can be reduced to enhance performance without compromising the mechanical robustness. With a further decrease in electrolyte thickness and operating temperature, current-collecting materials cheaper than platinum, such as silver and nickel, may become viable.

Benefiting from the 3D SOC's remarkable potential for enhanced compactness, reduced electrolyte thickness and elimination of metallic interconnects, we anticipate that these will offer substantial support and promising prospects for applying SOCs in the transportation, aerospace and portable device fields.

## Methods

### 3D structure design

The 3D gyroid unit model was designed using Creo Parametric software (version 7.0.2.0), featuring dimensions of 4 × 4 × 4 $mm^3$ and a wall thickness (gyroid electrolyte) of 0.2 mm. A monolithic SOC frame model was developed by increasing the number of gyroid units and adding an outer shell for gas sealing. Due to the maximum projected area width of 12 mm for our DLP printer, the monolithic SOC is designed with a diameter ranging from 10.0 to 10.6 mm (varying with different support/sealing thicknesses) and a height of 10.2 mm, where the sealings on the top and bottom are each 0.3-mm thick (Supplementary Fig. 1b). This design incorporates approximately 22.5 gyroid units. Obtuse angles of 135° are designed at the corners to mitigate stress concentration caused by sintering shrinkage. Samples with 0.3 mm thick supports were employed for electrochemical testing. Additionally, we have fabricated samples with varying support thicknesses specifically for compression testing, which will allow us to evaluate the impact of support thickness on their mechanical properties (Fig. 5a).

### DLP-based vat photopolymerization 3D printing

The DLP-based vat photopolymerization system[22], developed at DTU Construct, was used to manufacture all the samples. The system was in a UV-protected room with filters that eliminate short-wavelength light, preventing unintended curing due to environmental light exposure. The UV light is produced by the projection engine (Luxbeam LRW-WQ,

380 nm wavelength). With a projection lens, the UV light is focused on the surface of the building plate, curing the slurry and forming the cured parts on the building plate (Supplementary Fig. 1g). The building plate was coated with photo resin (cured) to enhance the adhesion during fabrication. A metal frame fixed a transparent FEP membrane on top of the glass. The membrane allows UV light to go through and allows for a delicate detachment of the part from the substrate. The pixel size is 7.54 µm. The thickness of a single layer was set at 10 µm. The bright regions in the slices were designed to be cured by UV light, whereas the dark regions were protected from curing with digital masks in the DLP projector. The curable slurry was made by mixing 8 mol% yttria-stabilized zirconia (8YSZ) powders, photo resin, dispersant and fine tuners. The commercial 8YSZ powders with a specific surface area of 16 ± 3 $m^2 g^{-1}$ from TOSOH company were used to prepare the slurry. The 8YSZ powders were mixed with a commercial photo resin from the 3Dresyn company, which incorporated dispersants and fine tuners FT1 and LB1, to create a slurry containing 37% by volume of 8YSZ powders. A light energy input ($E_i$) of 42 mJ $cm^2$ was utilized to cure the initial 15 layers, ensuring a robust attachment to the building plate. An $E_i$ of 36 mJ $cm^2$ for the subsequent feature layers was applied to maintain high resolution.

### Sample cleaning

Before proceeding with the subsequent heat treatment (that is, debinding and sintering), it is essential to thoroughly clean the residual slurry from the internal channels of the sample. Samples were placed in a beaker filled with the cleaner LithaSol 20 by Lithoz GmbH. Then, put the beaker into the water bath with a pre-heating of 40 °C and a frequency of 37 kHz. Refresh the cleaner and rinse the sample every 5 min. Repeat the process until no white 8YSZ slurry can be observed in the cleaner. Finally, an air gun was utilized to aid in expelling the residual cleaner liquid from the internal channels of the samples. The cleaned 3D-printed green parts are shown in Supplementary Fig. 1c.

### Debinding and sintering

The debinding and sintering process for the samples was carried out in a Sandberg chamber furnace with an allowed maximal operating temperature of 1,700 °C, under continuous ventilation, with no applied loads (free sintering) and within an air atmosphere. The heat treatment process parameters are depicted in Supplementary Fig. 1h. During the heat treatment, the samples stand in an alumina boat with 8YSZ powders (the same powders as the samples) evenly spread on the bottom.

### Electrodes slurry preparation and coating process

NiO-YSZ (1:1 in mass) and LSM-YSZ (1:1 in mass) were prepared as the powder-based slurry precursors of the fuel and oxygen electrodes, respectively. LSM is lanthanum strontium manganite with the equation of $(La_{0.80}Sr_{0.20})_{0.95}MnO_{3-x}$. YSZ is the 8YSZ, the same as the electrolyte. The slurry includes the binder, solvent, dispersant and powders. The mass fractions of the powders are 74 wt% and 65 wt% for the NiO-YSZ and LSM-YSZ, respectively. An air jet-assisted wet coating method was designed to coat electrodes on the gyroid electrolyte surfaces. Supplementary Fig. 4a shows the steps of the coating process. First, the channels of the sample were filled with slurry through injection. Next, an air gun applied a consistent pressure airflow (5 bar) to the channel entrance. Consequently, the remaining slurry in the channel was discharged with the aid of the gas pressure. Repeat operations were needed on various entrances until no discharged slurry could be observed. Finally, a thin-layer green electrode was formed on the gyroid electrolyte surface based on the adhesion of the slurry.

### Co-sintering of the coatings

Considering the higher sintering temperature required for NiO-YSZ compared to LSM-YSZ, the NiO-YSZ electrode was prepared before the LSM-YSZ electrode. For the NiO-YSZ electrode, the first coating underwent calcination at 1,000 °C for 1 hour. Then, the second coating was applied to the first calcined layer and treated at 1,000 °C for 1 hour. Subsequently, after the final layer was applied, the entire fuel electrode was sintered at 1,320 °C for 2 h. For the LSM-YSZ electrode, the pre-sintering of 900 °C for 1 hour was applied for the first two coatings, and the sintering of 1,150 °C for 2 h was applied for the whole sample after coating the final layer. After each heat treatment, the NiO-YSZ electrode shows an average single-layer mass gain of 77.9 ± 7.1 mg, whereas the LSM-YSZ electrode exhibits 72.5 ± 8.2 mg. The samples' mass gain represents a thickening of the electrode. Before conducting the full-cell electrochemical test, a platinum (Pt) paste from the Ferro GmbH company was applied to the electrode surfaces as the current collector. The channels were filled with Pt paste. Then, an airflow was used to discharge the residual Pt paste into the channels. This method is the same as that for coating the electrodes. Subsequently, the coated sample underwent calcination at 950 °C for 2 h. Silver paste from the SPI-CHEM company was mainly applied to the conductivity test (Supplementary Fig. 3d). The coating process is the same as that of the Pt coating. The Ag-coated sample underwent calcination at 800 °C for 2 h.

### Structure and microstructure characterization

The Nikon XTH 225 µfocus X-ray CT system was employed to characterize the samples in three-dimensional views. The operating parameters for the µCT scan were set at 215 kV, a power output of 6.5 W and a current of 30 µA, with a 0.25-mm filter made of Stannum (Sn) positioned between the X-ray source and the sample. The voxel size for the 3D-printed green parts is approximately 6.4 µm, whereas it is about 4.7 µm for the sintered parts. Avizo 9.4 software was used to analyse the µCT reconstruction. A Zeiss Ultra SEM was used to observe the microstructure features that exceed the µCT's resolution. The typical acceleration voltage employed for SEM and EDS observation/detection is within the range of 15–20 kV, accompanied by a working distance of 7.0–8.0 mm. A Leica optical microscope (OM) and a Leica digital camera captured the macro morphology of the samples.

### Compression test

The mechanical robustness of the 3D-printed monolithic SOCs with different support thicknesses was evaluated with the compression test performed on a 30 kN Zwick Roell universal testing machine with a loading rate of 0.001 mm $s^{-1}$. All samples possess the same electrolyte thickness of around 148 µm.

### Electrochemical testing for full 3D SOCs

The sample was secured on the testing platform, after which the entire assembly was subsequently positioned within the furnace, as depicted in Supplementary Fig. 5. The sample was connected to a Gamry 600 electrochemical workstation outside the furnace through the testing platform, enabling the monitoring of the sample's electrochemical performance. Gold and nickel meshes were directly connected to the electrochemical workstation, serving as the oxygen and fuel electrodes' current collectors, respectively.

The testing platform used for our samples is designed for normal-sized planar SOC at DTU, featuring an effective area of 4 × 4 $cm^2$. Modifications were made to the apparatus to make the sample holder fit the testing of our samples. First, platinum (Pt) separators were set up, as shown in Supplementary Fig. 5c. The separators transform the horizontal gas flow into a vertical one, facilitating the gas's entry into the channels of the vertically positioned sample. Additionally, they serve to separate the inlet and outlet gas streams. The separators were manufactured by applying a platinum paste to the designated area and then calcining it at 900 °C to form the desired structure.

Moreover, we also produced similar separators in the nickel mesh (Supplementary Fig. 5a). Second, a $ZrO_2$ mask was used to hold the sample. A hole in the $ZrO_2$ mask's centre corresponds to the position of

the sample's gas channel and the separators in the grooves of the nickel plate. By applying a combined load of 10 kg (comprising 2 kg from Load 1 and 8 kg from Load 2), the gold rings function as gas seals, effectively filling the gaps between the $ZrO_2$ mask and the holder (Sealing 1) and between the $ZrO_2$ mask and the sample (Sealing 2). The carbon tape (Supplementary Fig. 5d) was used to fix the sample before applying weight. The carbon tape can be burned off during the heating.

The SOFC mode was tested with gas flow rates set at 30 l $h^{-1}$ for the fuel electrode (wet $H_2$) and the oxygen electrode ($O_2$). The wet $H_2$ was obtained by passing $H_2$ through a bottle of water at room temperature; thus around 3% $H_2O$ was contained in the atmosphere. Three gas channels are utilized on the fuel gas side, and the effective gas supply rate can be estimated as 3/19 of the total gas supply rate (Supplementary Fig. 5c). The actual gas flow rate for the fuel electrode is estimated at 4.7 l $h^{-1}$. When accounting for the effective area of the fuel electrode (around 2.53 $cm^2$), the gas flow rate per unit area amounts to 1.9 l $(h\ cm^2)^{-1}$. This value is consistent with the $H_2$ flow rate of 1.5–1.88 l $(h\ cm^2)^{-1}$ used for normal-sized (4 × 4 $cm^2$) SOFC at DTU.

The SOEC mode was tested with the $O_2$ flow rate set at 30 l $h^{-1}$ for the oxygen electrode. Mixture atmospheres of hydrogen and steam with different ratios (60%$H_2$–40%steam, 50%$H_2$–50%steam and 10%$H_2$–90%steam) were supplied to the fuel electrodes of different samples. The mixed atmospheres were obtained by reacting $H_2$ with $O_2$ (the reaction occurred before entering the inlet of the gas channel). The data shown in Fig. 3e,f was obtained from the test using 60%$H_2$–40%steam with a set flow rate of 30 l $h^{-1}$ (the actual flow rate = 4.7 l $h^{-1}$); the data shown in Fig. 4b was obtained from the test using 50%$H_2$–50%steam with a set flow rate of 24 l $h^{-1}$ (the actual flow rate = 3.8 l $h^{-1}$); the data shown in Fig. 4c,d were obtained from the test using 10%$H_2$–90%steam with a set flow rate of 13.4 l $h^{-1}$ (the actual flow rate = 2.1 l $h^{-1}$).

Electrochemical characterization methods, including electrochemical impedance spectroscopy (EIS), voltage–current curve (IV) and galvanostatic test, were performed with a Gamry 600 electrochemical workstation. The 0.01–$10^6$ Hz frequency range and an amplitude voltage of 30 mV were used for EIS measurements of full 3D SOCs.

### Finite element simulation

Finite element simulations of the gyroid structure were performed using ANSYS software. The model employed 10-node tetrahedral elements, capable of capturing both elastic and plastic material behaviour, with each node accounting for displacements in the $x$, $y$ and $z$ directions. Due to the geometric complexity, the sub-modelling technique was applied. A mesh convergence study determined an optimal element size of 49 µm. The simulation process was carried out in two stages. Initially, a compression force representing the sealing load was applied to the entire gyroid structure using a coarser mesh. This preliminary analysis identified the most critical location within the structure, situated in the upper half of the gyroid. Subsequently, a sub-model of this critical region was developed with a finer mesh to evaluate the stresses induced by the sealing load. This approach ensured a precise and reliable analysis of the structural response.

## Data availability

All relevant data for this work can be found in the paper and Supplementary Information. A detailed overview of the data and plots are available at https://doi.org/10.11583/DTU.28153061. Source data are provided with this paper.

## References


1. Hauch, A. et al. Recent advances in solid oxide cell technology for electrolysis. *Science* **370**, eaba6118 (2020).
2. Wachsman, E. D. & Lee, K. T. Lowering the temperature of solid oxide fuel cells. *Science* **334**, 935–939 (2011).
3. Guan, D. et al. Hydrogen society: from present to future. *Energy Environ. Sci.* **16**, 4926–4943 (2023).
4. Abdelkareem, M. A. et al. On the technical challenges affecting the performance of direct internal reforming biogas solid oxide fuel cells. *Renew. Sustain. Energy Rev.* **101**, 361–375 (2019).
5. Wachsman, E. D., Marlowe, C. A. & Lee, K. T. Role of solid oxide fuel cells in a balanced energy strategy. *Energy Environ. Sci.* **5**, 5498–5509 (2012).
6. Hecht, M. et al. Mars Oxygen ISRU Experiment (MOXIE). *Space Sci. Rev.* **217**, 9 (2021).
7. Cable, T. L. & Sofie, S. W. A symmetrical, planar SOFC design for NASA's high specific power density requirements. *J. Power Sources* **174**, 221–227 (2007).
8. Hoffman, J. A. et al. Mars Oxygen ISRU Experiment (MOXIE)—preparing for human Mars exploration. *Sci. Adv.* **8**, eabp8636 (2022).
9. ElcoStack E3000 (fuel cell). *Elcogen* https://elcogen.com/products/solid-oxide-stacks-for-fuel-cell-systems/ (2024).
10. Lentatek solid oxide fuel cell (SOFC) stack. *Lentatek* https://www.lentatek.com/en/solutions/hydrogen-and-fuel-cell-technologies (2024).
11. Wobogroup SOFC stacks. *Wobogroup* https://wobogroup.en.made-in-china.com/product/OJCpGYjynLrX/China-Fuel-Cells-100kw-High-Efficiency-Solid-Oxide-Fuel-Cell-Stack.html (2024).
12. E&KOA SOFC stack, solid oxide fuel cell stack AERIE 120 (4kW). *Hyfindr* https://hyfindr.com/en/shop/products/solid-oxide-fuel-cell-stack-aerie-120 (2024).
13. Kyocera SOFC stack. *Kyocera* https://global.kyocera.com/prdct/ecd/sofc/ (2024).
14. Hayashi, K., Yokoo, M., Yoshida, Y. & Arai, H. Solid oxide fuel cell stack with high electrical efficiency. *NTT Tech. Rev.* **7**, 14–18 (2009).
15. De Bruijn, F. The current status of fuel cell technology for mobile and stationary applications. *Green Chem.* **7**, 132–150 (2005).
16. Singhal, S. C. Solid oxide fuel cells for stationary, mobile, and military applications. *Solid State Ion.* **152-153**, 405–410 (2002).
17. Boldrin, P. & Brandon, N. P. Progress and outlook for solid oxide fuel cells for transportation applications. *Nat. Catal.* **2**, 571–577 (2019).
18. Du, Y. & Finnerty, C. Tubular electrochemical cell. US patent 8,182,959 B2 (2012).
19. Tietz, F., Buchkremer, H. P. & Stöver, D. Components manufacturing for solid oxide fuel cells. *Solid State Ion.* **152-153**, 373–381 (2002).
20. Tarancón, A. et al. 2022 roadmap on 3D printing for energy. *J. Phys. Energy* **4**, 011501 (2022).
21. Maines, E. M., Porwal, M. K., Ellison, C. J. & Reineke, T. M. Sustainable advances in SLA/DLP 3D printing materials and processes. *Green. Chem.* **23**, 6863–6897 (2021).
22. Ribó, M. N. *Vat Photopolymerization Process Chain*. PhD thesis, Technical University of Denmark (2020).
23. Yuan, J. et al. 3D printing of robust 8YSZ electrolytes with a hyperfine structure for solid oxide fuel cells. *ACS Appl. Energy Mater.* **6**, 4133–4143 (2023).
24. Jia, K. et al. A new and simple way to prepare monolithic solid oxide fuel cell stack by stereolithography 3D printing technology using 8 mol% yttria stabilized zirconia photocurable slurry. *J. Eur. Ceram. Soc.* **42**, 4275–4285 (2022).
25. Martos, A. M. et al. 3D printing of reversible solid oxide cell stacks for efficient hydrogen production and power generation. *J. Power Sources* **609**, 234704 (2024).
26. Minh, N. Q. Ceramic fuel cells. *J. Am. Ceram. Soc.* **76**, 563–588 (1993).
27. Schoen, A. H. Infinite periodic minimal surfaces without self-intersections (NASA, 1970); https://ntrs.nasa.gov/citations/19700020472

28. Fischer, W. & Koch, E. On 3-periodic minimal surfaces. *Z. Kristallogr. Cryst. Mater.* **179**, 2031–2052 (1987).
29. Werner, J., Rodríguez-Calero, G., Abruña, H. & Wiesner, U. Block copolymer derived 3-D interpenetrating multifunctional gyroidal nanohybrids for electrical energy storage. *Energy Environ. Sci.* **11**, 1261–1270 (2018).
30. Maurel, A. et al. Toward high resolution 3D printing of shape-conformable batteries via vat photopolymerization: review and perspective. *IEEE Access* **9**, 140654–140666 (2021).
31. Dixit, T., Al-Hajri, E., Paul, M. C., Nithiarasu, P. & Kumar, S. High performance, microarchitected, compact heat exchanger enabled by 3D printing. *Appl. Therm. Eng.* **210**, 118339 (2022).
32. Pesce, A. et al. 3D printing the next generation of enhanced solid oxide fuel and electrolysis cells. *J. Mater. Chem. A* **8**, 16926–16932 (2020).
33. Trussler, S. Placement of reference electrode, electrolyte thickness and three-electrode cell configuration in solid oxide fuel cells: a brief review and update on experimental approach. *J. Electrochem. Soc.* **164**, F834–F844 (2017).
34. ElcoStack E3000 (electrolyzer). *Elcogen* https://elcogen.com/products/solid-oxide-stacks-for-electrolyser-systems/ (2024).
35. E&KOA SOEC stack. *Enkoa* https://www.enkoa.co.kr/page/product (2024).
36. Lira, M. et al. Large-area 3D printed electrolyte-supported reversible solid oxide cells. *Electrochim. Acta* **467**, 143074 (2023).
37. Zhou, Z., Nadimpalli, V. K., Pedersen, D. B. & Esposito, V. Degradation mechanisms of metal-supported solid oxide cells and countermeasures: a review. *Materials* **14**, 3139 (2021).
38. Monaco, F. et al. Degradation of Ni-YSZ electrodes in solid oxide cells: impact of polarization and initial microstructure on the Ni evolution. *J. Electrochem. Soc.* **166**, F1229 (2019).
39. Wang, Y. et al. Ni migration of Ni-YSZ electrode in solid oxide electrolysis cell: an integrated model study. *J. Power Sources* **516**, 230660 (2021).
40. Shang, Y. *Microstructure Evolution of Ni-yttria Stabilized Zirconia Electrodes for Solid Oxide Electrolysis Cells: Experimental Characterization and Phase Field Modeling*. PhD thesis, Technical University of Denmark (2024).
41. Cui, T., Xiao, G., Yan, H., Zhang, Y. & Wang, J. Q. Numerical simulation and analysis of the thermal stresses of a planar solid oxide electrolysis cell. *Int. J. Green. Energy* **20**, 432–444 (2023).


## Acknowledgements

We acknowledge DTU colleagues H. Henriksen, R. Caldogno, A. Danielak, C. Grundlach, S. Baier, S. Wang, B. Liu, L. Knudsen and E. Abdellahi for their assistance with equipment training and experiments. We acknowledge the financial support from the China Scholarship Council (grant number 202006370033, Z.Z. and V.E.), the Danish national VILLUM P2X Accelerator Program (grant number VPX-08, V.E., Z.Z., V.K.N. and D.B.P.) and the Poul Due Jensen Foundation for funding the project titled 'Open Additive Manufacturing Initiative' (grant number 2018-017, V.K.N. and D.B.P.) for supporting this research.

## Author contributions

Conceptualization: V.E. and Z.Z. Methodology: Z.Z., V.E. and V.K.N. Investigation: Z.Z., A.R.L., Z.P., P.S., Y.X., Y.S., A.B., N.S., M.A., V.K.N. and J.L.N. Visualization: Z.Z., A.R.L., Z.P., V.B.T., Y.S., V.K.N. and V.E. Funding acquisition: Z.Z., V.K.N., D.B.P. and V.E. Project administration: V.E. Supervision: V.E. and V.K.N. Writing—original draft: Z.Z., V.E., P.S., V.K.N. and V.B.T. Writing—review and editing: Z.Z., V.E., V.B.T., X.S., P.S., V.K.N. and all. Resources: P.S., Y.X., A.B., P.K. and M.C.

## Competing interests

The authors declare no competing interests.

## Additional information

**Supplementary information** The online version contains supplementary material available at https://doi.org/10.1038/s41560-025-01811-y.

**Correspondence and requests for materials** should be addressed to Zhipeng Zhou, Venkata K. Nadimpalli or Vincenzo Esposito.

**Peer review information** *Nature Energy* thanks Yanhai Du, Inyoung Jang and the other, anonymous, reviewer for their contribution to the peer review of this work.